Nanoscale Advances

ROYAL SOCIETY OF CHEMISTRY

PAPER

View Article Online
View Journal | View Issue



Cite this: *Nanoscale Adv.*, 2022, **4**, 2816

# A van der Waals heterojunction based on monolayers of $MoS_2$ and $WSe_2$ for overall solar water splitting†

Paul Dalla Valle * and Nicolas Cavassilas

Received 24th March 2022
Accepted 29th April 2022

DOI: 10.1039/d2na00178k

rsc.li/nanoscale-advances

Solar water splitting (SWS) has been widely studied as a promising technology for generating carbon-free hydrogen. In this article, we propose an unassisted SWS system based on van der Waals heterojunctions using monolayers of transition metal dichalcogenides as active core materials. This architecture, with its small band gap materials and high surface/volume ratio, has an intrinsic type-II band alignment that offers many advantages, such as direct Z-scheme configuration and wide absorption. To estimate the solar-to-hydrogen (STH) efficiency of the system, we developed a multiphysics model. While electronic and optical properties are computed with *ab initio* calculations, we implemented the detailed balance method and the Butler–Volmer kinetics to simulate the photoelectrochemical behaviour. Under realistic operating conditions, the system achieves a STH efficiency greater than 15%, which is higher than the critical 10% efficiency required to make SWS economically viable. Since our system is wireless and requires simple manufacturing processes (exfoliation), this result is remarkable.



## 1 Introduction

Sunlight is an abundant, renewable and inexpensive source of energy and is therefore a competitive alternative to fossil fuels in the current energy crisis. However, because of its intermittency, it is necessary to store this energy. Solar water splitting (SWS) is a photoelectrochemical process which converts solar energy into chemical energy by producing hydrogen, a compound with high energy density. As its combustion does not release harmful greenhouse gases, hydrogen appears as a promising and clean energy vector for the future.[1] The basic principle of SWS requires a bias of 1.23 V between two electrodes immersed in water. In overall water splitting process, $H_2$ and $O_2$ are produced simultaneously in 2 : 1 stoichiometric ratio by the cathode and the anode respectively.[1] Actually, considering the various intrinsic losses in the system (such as the catalytic overpotentials), the bias required for SWS is reported as 1.6–2.4 V.[2] To achieve this bias while maximising the absorption of sunlight, a two-step photoexcitation process, known as Z-scheme, is an attractive solution.[3] Over the past few years, many researches focused on the investigation and development of Z-scheme photoelectrochemical cells for SWS. These researches have been compiled in several reviews.[4–6]

To improve the electrochemical reactions in the overall water splitting process, the generation of electron–hole pairs must occur as close to the surface as possible. Thanks to their large surface/volume ratio, two-dimensional (2D) materials, such as transition metal dichalcogenide (TMDC) seem perfectly suited for this purpose. As reviewed by Das *et al.*, TMDC and their van der Waals heterojunctions (vdWH) are attractive for photovoltaic applications[7] thanks, in particular, to their remarkable optical properties[8–12] and Z-scheme architectures based on TMDC vdWH have already been proposed.[13–16] Also, 2D TMDC present appealing catalytic properties.[17,18] Yin *et al.* reviewed applications such as the electrocatalytic hydrogen evolution reaction and photocatalysis[19] while Wu *et al.* demonstrated the catalytic performance of $MoS_2$ in oxygen evolution reaction, which is comparable to the benchmark $IrO_2$.[18] Interestingly, these photocatalytic properties can be enhanced by chalcogen vacancy of the TMDC monolayer.[20] Moreover, the production of 2D TMDC is low-cost thanks to the exfoliation process.[17,21,22] Consequently, the use of these vdWH is increasingly considered as a credible alternative for the overall SWS, as evidenced by theoretical papers showing high efficiencies.[20,23] In this paper, we present a direct Z-scheme system based on a $MoS_2/WSe_2$ vdWH. We go beyond the presentation of the potential performances of the heterojunction as we propose a complete design of the photoelectrochemical cell. The active core of the cell contains the vdWH and an insulating layer to prevent unwanted recombinations. This active core is embedded in transparent insulating layers which are porous to enable the circulation of water and gases. To investigate our system, we calculate the electronic properties of the heterojunctions with density

*Aix Marseille Université, CNRS, Université de Toulon, IM2NP UMR 7334, 13397, Marseille, France. E-mail: paul.dalla-valle@im2np.fr*

† Electronic supplementary information (ESI) available: Absorbance formula, justification of the external radiative efficiency hypothesis, *ab initio* methods, TMDC band structures, modelling of the absorption enhancement system, influence of the intrinsic parameters. See https://doi.org/10.1039/d2na00178k

functional theory (DFT). Based on these results, we implement a photoelectrochemical model using the detailed balance method and the Butler–Volmer kinetics to compute the solar-to-hydrogen (STH) efficiency under realistic conditions. In the following section, we describe the system operation. We then detail the developed photoelectrochemical model. We finally present and discuss the calculated STH efficiency of the system.

## 2 System operation

Our system, depicted in Fig. 1(a), is based on a $MoS_2/WSe_2$ vdWH where $MoS_2$ and $WSe_2$ are used as the anode and the cathode respectively. Two distinct regions form its active core. Fig. 1(b) represents the band diagram of the $MoS_2$/hBN/$WSe_2$ vdWH which composes the first region. Hexagonal boron nitride (hBN) is a large gap insulator ($E_g > 6$ eV).[24] As for TMDCs, one can produce monolayers of hBN by simple exfoliation[25] and these monolayers can form vdWH with TMDCs.[26] In the first region, $MoS_2$ and $WSe_2$ are isolated by hBN and are thus independent. Each TMDC absorbs a fraction of the incident light and generates electron–hole pairs. The hydrogen evolution reaction consumes the electron at the cathode ($WSe_2$) while the oxygen evolution reaction uses the hole at the anode ($MoS_2$). These two electrochemical reactions require suitable band edge positions, that is the valence band maximum (VBM) of $MoS_2$ must be lower $E_{H_2O/O_2}$, the redox potential of $H_2O/O_2$, while the conduction band minimum (CBM) of $WSe_2$ must be higher $E_{H^+/H_2}$ the redox potential of $H^+/H_2$. As shown in Fig. 1(b), we note $\chi_{O_2}$ ($\chi_{H_2}$) the energy difference between the VBM (CBM) of $MoS_2$ ($WSe_2$) and $E_{H_2O/O_2}$ ($E_{H^+/H_2}$). According to this definition, for proper operation of the device, $\chi_{O_2}$ must be negative while $\chi_{H_2}$ must be positive. In this first region, hBN prevents electrons in the conduction band of $WSe_2$ from relaxing into the conduction band of $MoS_2$ and also prevents holes in the valence band of $MoS_2$ from relaxing into the valence band of $WSe_2$. Fig. 1(c) presents the band diagram of the heterojunction in the second region where hBN is removed to form a $MoS_2/WSe_2$ vdWH. The recombination of the extra carriers generated in the first region (*i.e.* the electrons of $MoS_2$ and the holes of $WSe_2$) takes place in this second region. The extra carriers must diffuse from a region with hBN to a region without. This recombination is mandatory to avoid an accumulation of carriers which would stop the SWS process. In the results section, and in particular in the *ab initio* calculation section, we will see that the hybridisation of the electronic states in the valence band of the TMDCs ensures the recombination. Valence states of $WSe_2$ are delocalized in $MoS_2$ and create states in the band gap of the latter.[27] We can explain this hybridisation considering that two 2D TMDCs, forming a vdWH, create a new specific material that cannot be described by the simple superposition of the two TMDCs. Concerning the $MoS_2/WSe_2$ couple, our calculation reveals delocalized states that are beneficial to the device operation because they favour the recombination of the extra carriers.

One must encapsulate the ultra-thin active core to protect and support it without avoinding the circulation of water and gases. To this end, mesoporous transparent oxides[28] appear as good option. Also, high-quality optical absorption in the TMDCs is essential as their ultimate thinness remains limiting. Many works have been interested in improving optical absorption in 2D materials, as presented in the review by Li *et al.*[29] The mesoporous oxides can serve as a support for absorption enhancement systems, such as photonic crystals, resonant cavities, nanoparticles.

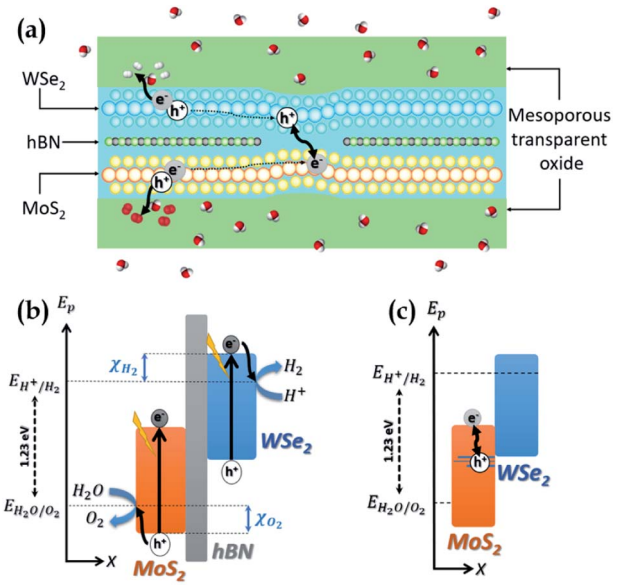


Fig. 1 (a) Schematic representation of the SWS system. The active core is based on a $MoS_2$/hBN/$WSe_2$ vdWH and a $MoS_2/WSe_2$ vdWH. A transparent mesoporous oxide supports and protects the active core. (b) Sketch of the band diagram in the first region where the $MoS_2$ and $WSe_2$ are isolated by hBN. $E_{H^+/H_2}$ and $E_{H_2O/O_2}$ are respectively the reaction potentials of the reduction of $H^+$ in $H_2$ and of the oxidation of $H_2O$ and $O_2$. This region is the seat of carrier generation and electrochemical reactions. (c) Sketch of the band diagram in the second region, without hBN. This region enables the recombination of the excess carriers.

## 3 Model

To estimate the realistic efficiency of our system, we have developed a detailed balance model based on *ab initio* calculations. The foundation of this model is inspired by the work of Fountaine *et al.*[30] We first compute an inverse formulation of the current–voltage characteristic of a photoelectrochemical system, $V_{PEC}(J)$,

$$V_{PEC}(J) = V_{MoS_2}(J) + V_{WSe_2}(J) - V_{MoS_2/WSe_2}(-J) - V_{cat,a/c}(J) \geq E_{rxn} \quad (1)$$

where $V_{PEC}$ is the voltage available for the electrochemical reaction and $J$ is the current density. Fig. 2 shows the different voltages of eqn (1). In this equation, the positive terms are the voltages generated by the TMDCs ($V_{MoS_2}$ and $V_{WSe_2}$) when they are isolated by hBN and the negative terms are the intrinsic losses of the system. These losses are the catalytic overpotentials at the anode and the cathode ($V_{cat,a}$ and $V_{cat,c}$ respectively) and the voltage drop $V_{MoS_2/WSe_2}$ generated by the

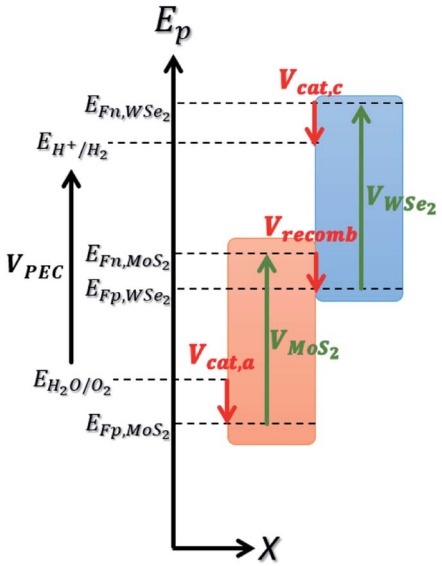


Fig. 2 Representation of the different voltages involved in the computation of $V_{PEC}$, depicted on the band diagram of the $MoS_2/WSe_2$ heterojunction. The green arrows represent the voltages generated by the devices. Red arrows represent the losses induced by catalytic overpotentials and carrier's recombination in the region without hBN. $E_{Fn}$ and $E_{Fp}$ represent the energy of the pseudo-Fermi level of electrons and holes respectively.

recombination of carriers in the $MoS_2/WSe_2$ heterojunction (*i.e.* the region without hBN). In this model, we only consider the intrinsic losses of the system, we thus neglect the series resistance which is related to the ionic transportation in the electrolyte.

The voltage $V_{PEC}$ must be greater than or equal to the electrochemical reaction potential for the reaction to take place. For water electrolysis, this potential is $E_{rxn} = 1.23$ V.

We compute the current–voltage characteristics of the isolated $MoS_2$, the isolated $WSe_2$ and the $MoS_2/WSe_2$ heterojunction to calculate $V_{MoS_2}(J)$ and $V_{WSe_2}(J)$ and $V_{MoS_2/WSe_2}(J)$ respectively. To this end, we use a detailed balance model based on the balance between the generation and the recombination rates of the electron/hole pairs. The carrier generation rate $G_{TMDC}$ is the number of electron–hole pairs photogenerated in the TMDC per unit of volume and time. Here, "TMDC" refers to either $MoS_2$, $WSe_2$ or the $MoS_2/WSe_2$ heterojunction. $G_{TMDC}$ depends on the number of incident photons and the absorption of these photons. In this paper, we use the AM1.5 G solar spectrum. The generation rate is given by the expression

$$G_{TMDC} = \frac{1}{q}\int_0^\infty \frac{\text{AM1.5 G}(E)}{E} \times \frac{A_{TMDC}(E)}{L_{TMDC}} \times dE \quad (2)$$

where $q$ is the elementary charge, $E$ is the energy of the photon, $A_{TMDC}(E)$ is the absorbance of the TMDC and $L_{TMDC}$ is its thickness.

The absorbance $A_{TMDC}(E)$ is a function of the absorption coefficient of the materials and the geometry of the active core. We use DFT to compute the *ab initio* absorption coefficients of $MoS_2$, $WSe_2$ and the $MoS_2/WSe_2$ heterojunction. The complete expression of $A_{TMDC}(E)$ is presented in ESI 1.†

The carrier recombination rate $R_{TMDC}$ is the number of recombination of electron–hole pairs in each TMDC per unit of volume and time. We use generalized Planck's law to describe spontaneous radiative recombination. To take into account the non-radiative recombination, we introduce an external radiative efficiency coefficient (ERE)[31] in the calculation of $R_{TMDC}$. The latter is given by

$$R_{TMDC} = \int_0^\infty \frac{\alpha_{TMDC}(E)}{ERE} \times \frac{8\pi n_{op,TMDC}^2}{c^2\hbar^3} \times \frac{E^2}{\exp\left(\frac{E - qV_{TMDC}}{kT}\right) - 1} dE \quad (3)$$

where $\alpha_{TMDC}(E)$ is the absorption coefficient, $n_{op,TMDC}$ is its the optical index, $c$ is the speed of light, $\hbar$ is the Planck constant, $k$ is the Boltzmann constant and $T$ is the device temperature.

As the recombination rate $R_{TMDC}$ depends on $V_{TMDC}$, we can define the current–voltage characteristic of a TMDC of thickness $L_{TMDC}$ as:

$$J(V_{TMDC}) = -q(G_{TMDC} - R_{TMDC}(V_{TMDC}))L_{TMDC} \quad (4)$$

We now introduce the parameter $\gamma$ which represents the fraction of the $MoS_2$/hBN/$WSe_2$ heterojunction in the active core. The proportion $1 - \gamma$ is thus the fraction of the region without hBN. In the region with the hBN, eqn (4) thus becomes

$$J(V_{TMDC}) = -q \times \gamma(G_{TMDC} - R_{TMDC}(V_{TMDC}))L_{TMDC} \quad (5)$$

and in the region without hBN it becomes

$$J(V_{HJ}) = -q \times (1 - \gamma)(G_{HJ} - R_{HJ}(V_{HJ}))L_{HJ} \quad (6)$$

where HJ refers to the $MoS_2/WSe_2$ heterojunction.

We numerically invert eqn (5) to get the relations $V_{MoS_2}(J)$ and $V_{WSe_2}(J)$, and we invert eqn (6) to get $V_{MoS_2/WSe_2}(J)$.

To determine the current dependence of the catalytic overpotentials we use an inverse formulation of the Butler–Volmer kinetics and we assume that the charge transfer coefficients at the anode and the cathode are equal ($\alpha_a = \alpha_c = \alpha$).[32] We implement the overpotentials of the anode and the cathode $V_{cat,a/c}(J)$ with the following expression,

$$V_{cat,a/c}(J) = \frac{R_m T}{\alpha n_e F} \sinh^{-1}\left(\frac{J}{2J_{0,a/c}}\right) \quad (7)$$

where $R_m$ is the universal gas constant, $F$ is the Faraday constant and $J_{0,a/c}$ is the catalytic exchange current density of the anode and the cathode respectively.

Once eqn (1) is implemented, we calculate the STH efficiency of the device. To do so, we first compute the optimal current density $J_{op}$, which is the maximum current density that satisfies the condition $V_{PEC}(J_{op}) \geq 1.23$ V. We get $\eta_{PEC}$, the STH efficiency, thanks to the following equation:

$$\eta_{STH} = \frac{J_{op}E_{rxn}}{P_{in}} \times f_{FE} \quad (8)$$

Table 1 Intrinsic parameters according to the three cases (no. 1: ideal materials, no. 2: high-performance materials and no. 3: standard quality materials)

| Case | ERE | $J_{0,a}$ (mA cm$^{-2}$) | $J_{0,c}$ (mA cm$^{-2}$) |
|---|---|---|---|
| No. 1 | 1 | $+\infty$ | $+\infty$ |
| No. 2 | $10^{-2}$ | $10^{-3}$ | 1 |
| No. 3 | $10^{-6}$ | $10^{-5}$ | 1 |

where $f_{FE}$ is the faradaic efficiency (assumed to be unitary in the rest of this article), and $P_{in}$ is the incident sun power, calculated using the AM1.5 G spectrum:

$$P_{in} = \frac{1}{q}\int_0^\infty \mathrm{AM1.5\ G}(E)\mathrm{d}E. \quad (9)$$

Before presenting the results of the model, we focus on its important parameters. We classify them into two categories: intrinsic parameters and parameters related to the design of the device. The first category accounts for the non-ideality of the materials and their heterojunctions and includes the external radiative efficiency (ERE) and the anodic and cathodic catalytic exchange current density ($J_{0,a}$ and $J_{0,c}$ respectively). These intrinsic parameters are specific to the materials and their manufacture and *a priori* unknown for our system. Inspired by the work of Fountaine *et al.*,[30] we distinguish three cases, summarised in Table 1, to study the STH efficiency of the device. Case no. 1 corresponds to the ideal limit case where each recombination is radiative (ERE = 1) and the overpotentials are zero (which corresponds mathematically to infinite catalytic exchange current densities). Case no. 2 is a realistic case with high radiative and electrochemical performances. Finally, case no. 3 accounts for average radiative and electrochemical quality. We assume that the external radiative efficiencies are equal for the isolated TMDCs and the heterojunction. We discuss the validity and the consequences of this assumption in ESI 2.†

The second category of parameters groups two design parameters: $\gamma$, the proportion of region with hBN and $N$, the absorption quality. We introduced $\gamma$ during the presentation of the model in eqn (5) and (6). $N$ represents the number of light passages through the device. It models, in a simplified manner, the absorption quality, which can be enlarged by considering for instance a photonic crystal, a resonant cavity and/or by considering several layers of the active core. We describe the influence of $N$ on the active core absorption in ESI 1.†

## 4 Results and discussion

In this section, we present the significant results in three steps. First, we show the *ab initio* results of band structures and absorption coefficients. We describe the computational methods used for these *ab initio* calculations in ESI 3.† Then we study the system efficiency *versus* the design parameters ($\gamma$ and $N$) according to the three cases (ideal, high performance and standard quality). Finally, we emphasise the influence of the intrinsic parameters (ERE and $J_{0,a/c}$) on the STH efficiency of the device.

We first present the *ab initio* band structure calculated with DFT. The band structures of the isolated materials are shown in ESI 4† and are in good agreement with the literature. From these band structures, we deduce $\chi_{O_2}$ and $\chi_{H_2}$ from the redox potentials $E_{H_2O/O_2}$ and $E_{H^+/H_2}$ respectively. These redox potentials have a bearing on the pH of water and are calculated with the following expression,[23]

$$E_{H_2O/O_2} = -4.44\ \mathrm{eV} + \mathrm{pH} \times 0.059\ \mathrm{eV} \quad (10)$$

$$E_{H^+/H_2} = -5.67\ \mathrm{eV} + \mathrm{pH} \times 0.059\ \mathrm{eV} \quad (11)$$

where the energy reference is set to the vacuum level. At pH 0, we find $\chi_{O_2}$ and $\chi_{H_2}$ equal to −0.25 eV and 0.91 eV respectively. At pH 7, $\chi_{O_2}$ and $\chi_{H_2}$ are equal to −0.66 eV and 0.50 eV respectively. We use the isolated band structures to calculate $\chi_{O_2}$ and $\chi_{H_2}$ because the electrochemical reactions occur in the region with hBN (*i.e.* when the TMDC are isolated). We note that the catalytic overpotentials ($V_{cat,a/c}$) are not defined *versus* the band extremum, but *versus* the pseudo-Fermi levels. Then, $\chi_{O_2}$ and $\chi_{H_2}$ give the upper limit of $V_{cat,a/c}$, which is reached if the pseudo-Fermi levels are degenerated out of the band gap. This degeneracy occurs with a very efficient absorption, for instance.

Fig. 3 shows the projected band structure of the $MoS_2/WSe_2$ heterojunction. The red (blue) dots represent electronic states around the nuclei of $MoS_2$ ($WSe_2$). We first note that the band structure shows a direct band gap of 0.58 eV at the $K$ point of the first Brillouin zone. We identify the band edge electronic states mainly localised around $MoS_2$ or $WSe_2$ and thus find a type II (tandem) heterojunction. The band structure shows that the band gap of the $MoS_2$ is 1.46 eV and that of the $WSe_2$ is 1.88 eV. We note that these values are different from the gaps obtained for the isolated materials (ESI 4†) due to the stress induced by the heterojunction.[33] Finally, the most important point to note in this band structure is the state hybridisation in the valence band. Close to the VBM, the electronic states are localised around both $MoS_2$ and $WSe_2$. This hybridisation enables direct recombination of electrons and holes in $MoS_2$. Hence, we expect

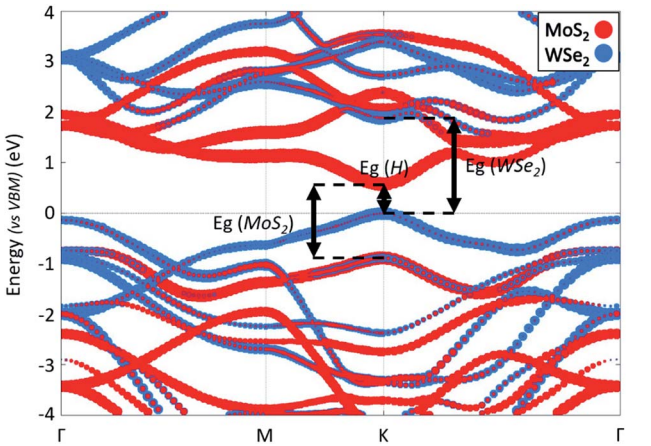


Fig. 3 Band structure of the $MoS_2/WSe_2$ heterojunction along a $\Gamma$–$M$–$K$–$\Gamma$ path. The energy reference is set to VBM. The red (blue) dots represent electronic states around the nuclei of $MoS_2$ ($WSe_2$).

radiative recombination with emission of photons of energy $E_g$ = 0.58 eV. This hybridization is confirmed by experimental results which show the existence of an interlayer exciton in this heterojunction.[27] Regarding both the band alignment and the type II configuration, the $MoS_2/WSe_2$ heterojunction fulfils the basic requirements of the overall water splitting.

Fig. 4 displays the *ab initio* absorption coefficients of the isolated $MoS_2$ and $WSe_2$ and their heterojunction. The absorption coefficient of the isolated monolayers, Fig. 4(a), shows that $MoS_2$ and $WSe_2$ have analogous behaviours around the band edges. This could be a problem in the case of a 3D heterojunction where the top material would absorb all the incident light. Due to their extreme thinness, the single-pass absorption of 2D TMDCs is less than 10%.[34] In a 2D vdWH, the top TMDC will absorb less than 10% of the incident light. The remaining more than 90% will be available for the bottom TMDC, which will in turn absorb 10%. Having two absorbers in the same energy range is therefore not a problem for the operation of the device. However, we will see below that we must enhance the total absorption to improve the efficiency of the system, *i.e.* we need more than a single-pass. Fig. 4(b), which represents the absorption coefficient of the $MoS_2/WSe_2$ heterojunction, shows that the absorption is non-zero for energy larger than 0.4 eV. Corresponding radiative recombination is thus expected.

Using these absorption coefficients and our multiphysics model, we calculate the system efficiency. Fig. 5 presents the STH efficiency $\eta_{STH}$ according to the design parameters for the

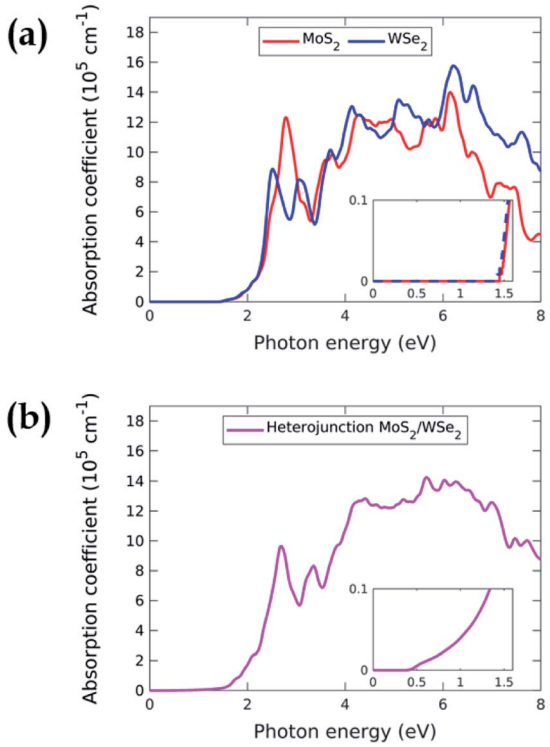


Fig. 4 (a) Absorption coefficient of $MoS_2$ (red curve) and $WSe_2$ (blue curve) *versus* the photon energy. (b) Absorption coefficient of the $MoS_2/WSe_2$ heterojunction. In both graphs, the inset plot is a zoom in the low energy range.

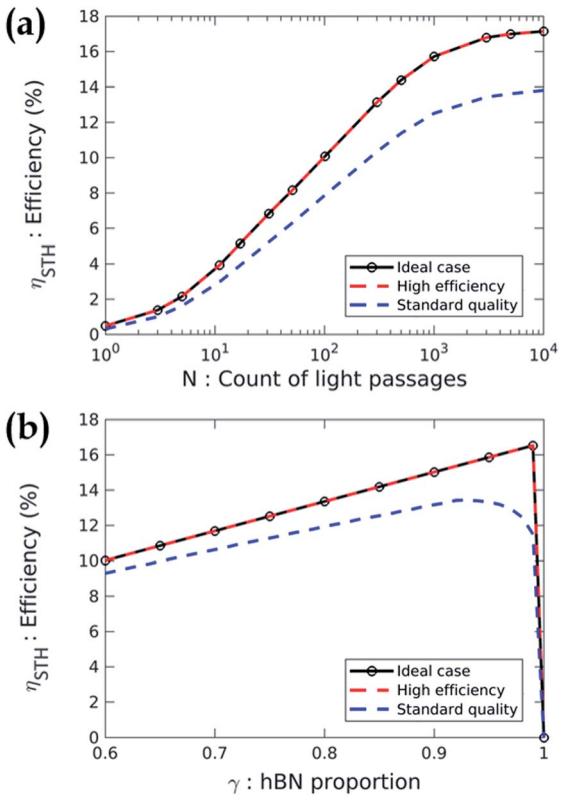


Fig. 5 (a) STH efficiency *versus* $N$, the absorption quality, according to three cases (ideal materials, high-efficiency materials and standard quality materials). $\gamma$ is set to 0.99 for ideal and high efficiency materials and set to 0.93 for standard quality materials (b) STH efficiency *versus* $\gamma$, the proportion of region with hBN, according to the same cases. Here, $N$ is set to 3001 for each case.

three cases previously described in Table 1. Fig. 5(a) shows a strong dependence of the efficiency with $N$. Without optical absorption enhancement (*i.e.* $N = 1$), the STH efficiency is less than 0.5% whatever the case. Hence, the development of high-performance absorption enhancement system is mandatory to get valuable efficiencies. At high absorption quality ($N > 1000$), the efficiency saturates because all the photons are absorbed. The efficiency is 17.2% in cases no. 1 and no. 2 and 13.8% in case no. 3. The absorption quality is then a key factor in the device performance. Indeed, for a constant incident power, better absorption generate more carriers and thus a larger current, which increases the STH efficiency (eqn (8)). Even if the parameter $N$ is a simplified way of describing the absorption, we use it to state that to reach 10% efficiency in case no. 3, the active core must absorb 71% of the photons with an energy higher than the band gap energy. In case no. 2, it has to absorb 56% of the incident light in the same energy range to reach the 10% efficiency. We present the detail of these statements in ESI 5.†

Fig. 5(b) depicts the STH efficiency *versus* the proportion of region with hBN. The result shows that $\gamma$ must be larger than 0.9 whatever the case. Indeed, increasing the proportion of the $MoS_2$/hBN/$WSe_2$ heterojunction increases the surface of the device dedicated to photon absorption and electrochemical

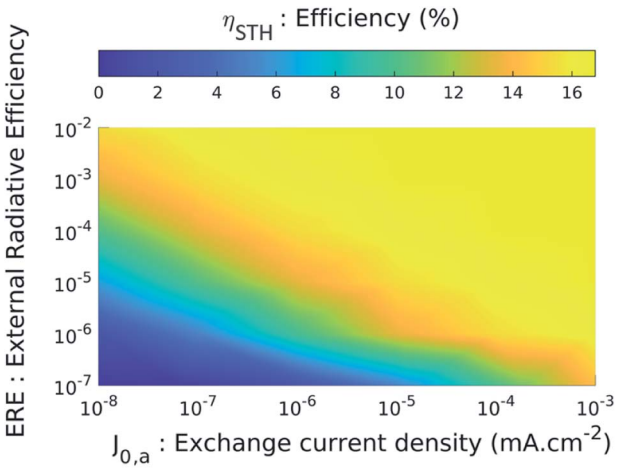


Fig. 6 STH efficiency *versus* two intrinsic parameters, the external radiative efficiency ERE and the anodic exchange current density $J_{0,a}$. Here, $N$ is set to 3001 and $\gamma$ is set to maximise the efficiency for each point ($\gamma$ lies between 0.82 and 0.99). $J_{0,c}$ is set according to case 2 (*i.e.* $J_{0,c} = 1$ mA cm$^{-2}$).

reactions. Moreover, the recombination in the region without hBN is sufficiently efficient to be non-limiting. However, if $\gamma$ is too close to 1, the efficiency drops to zero because there is not enough recombination of the excess carriers. This result is advantageous for the design of the device since one can imagine to randomly stack exfoliated flakes of $MoS_2$ then hBN and finally, $WSe_2$ to produce the active core. This non-ideal stacking will inevitably create some regions without hBN which will naturally enable the recombination of the carriers.

In both graphs of Fig. 5(a) and (b), we note that the curves representing cases no. 1 and no. 2 (*i.e.* the ideal case and the case of high-performance materials) are identical. To understand this result, we study the STH efficiency *versus* the intrinsic parameters. Fig. 6 shows $\eta_{STH}$ *versus* the external radiative efficiency ERE and *versus* the catalytic exchange current density at the anode $j_{0,c}$.‡ The efficiency is zero if the intrinsic parameters are too poor. Indeed, poor radiative efficiency (*i.e.* ERE $\ll 1$) leads to a low voltage generated by TMDCs and a poor catalytic behaviour (*i.e.* weak $j_{0,a/c}$) requires applying a larger overpotential to maintain a given current density. We refer the reader to ESI 6 and 7† for more details on the influence of radiative efficiency and the exchange current density respectively. The combination of these two phenomena leads to a voltage available for the electrochemical reaction too low to enable the electrolysis of water (we have $V_{PEC}(J) < 1.23$ V regardless of the current density), which gives a zero efficiency. This is the case for example if ERE $= 10^{-7}$ and $J_{0,a} = 10^{-8}$ mA cm$^{-2}$ where the maximum voltage that the system can deliver is 1.16 V. Conversely, beyond a certain quality of the materials, better intrinsic parameters do not improve the performance. The latter presents constant 16.4% efficiency (Fig. 6) which is reached when the following condition is observed: $J_{op} = \min(J_{SC,MoS_2}; J_{SC,WSe_2})$ where $J_{SC,MoS_2}$ and $J_{SC,WSe_2}$ are the short-circuit current densities of $MoS_2$ and of $WSe_2$ respectively. Once the efficiency reaches this limit, it is no longer useful to increase the voltages delivered by the cells or to decrease the losses.

‡ The cathodic exchange current density difference between standard and high-quality materials is negligible. It is not the case of the anodic exchange current density.

## 5 Conclusions and perspectives

In conclusion, we propose in this article a vdWH for overall water splitting. The bias is produced by $MoS_2$ and $WSe_2$ monolayers in a direct Z-scheme vdWH. The system is unassisted and is based on non-toxic, earth abundant materials. The photoelectrochemical model, based on *ab initio* results, shows a STH efficiency of more than 10% for standard photovoltaic and electrochemical quality materials. Since TMDCs are very promising for these applications, we can expect efficiencies over 15%. This efficiency exceeds the critical 10% efficiency required to make SWS economically viable.[20,35] The system requires simple manufacturing processes (exfoliation), which enables production of carbon-free hydrogen without using rare metals. This system can also be considered for decentralised production, which can be advantageous in remote places or for individual uses.

It is, however, important to note that the DFT calculations involve systematic errors, in particular in the computation of the band gap energies of the system.[36] These numerical results will have to be compared with experimental results of the optical properties of the 2D TMDCs (isolated and in heterojunction). These measurements will be the subject of future work. If the DFT calculations have underestimated the band gap energies too much, it will be possible to adjust the model with the new values. It is also conceivable to consider other TMDCs exhibiting photoelectrochemical properties similar to or better than those of this paper. We also note that in our study, the calculated band gaps of $MoS_2$ and $WSe_2$ are almost identical. This is not a necessary condition for the correct operation of the device. After selecting the active materials, it will be possible to carry out more in-depth and realistic modelling of the light management system. This point is crucial since the absorption quality is essential to obtain significant STH efficiency.

## Conflicts of interest

There are no conflicts to declare.

## Acknowledgements

The authors acknowledge the Centre de Calcul Intensif d'Aix-Marseille for granting access to its high-performance computing resources.

## Notes and references

1 R. Li and C. Li, *Advances in Catalysis*, Elsevier, 2017, vol. 60, pp. 1–57.

2 M. G. Walter, E. L. Warren, J. R. McKone, S. W. Boettcher, Q. Mi, E. A. Santori and N. S. Lewis, *Chem. Rev.*, 2010, **110**, 6446–6473.
3 Q. Xu, L. Zhang, J. Yu, S. Wageh, A. A. Al-Ghamdi and M. Jaroniec, *Mater. Today*, 2018, **21**, 1042–1063.
4 T. Hisatomi, J. Kubota and K. Domen, *Chem. Soc. Rev.*, 2014, **43**, 7520–7535.
5 Q. Wang and K. Domen, *Chem. Rev.*, 2020, **120**, 919–985.
6 J. Abdul Nasir, A. Munir, N. Ahmad, T. ul Haq, Z. Khan and Z. Rehman, *Adv. Mater.*, 2021, **33**, 2105195.
7 S. Das, D. Pandey, J. Thomas and T. Roy, *Adv. Mater.*, 2019, **31**, 1802722.
8 M. Amani, D.-H. Lien, D. Kiriya, J. Xiao, A. Azcatl, J. Noh, S. R. Madhvapathy, R. Addou, S. Kc, M. Dubey, K. Cho, R. M. Wallace, S.-C. Lee, J.-H. He, J. W. Ager, X. Zhang, E. Yablonovitch and A. Javey, *Science*, 2015, **350**, 1065–1068.
9 N. Ansari and E. Mohebbi, *Opt. Mater.*, 2016, **62**, 152–158.
10 C. Janisch, H. Song, C. Zhou, Z. Lin, A. L. Elías, D. Ji, M. Terrones, Q. Gan and Z. Liu, *2D Mater.*, 2016, **3**, 025017.
11 D. Jariwala, A. R. Davoyan, J. Wong and H. A. Atwater, *ACS Photonics*, 2017, **4**, 2962–2970.
12 Y. Li, A. Chernikov, X. Zhang, A. Rigosi, H. M. Hill, A. M. van der Zande, D. A. Chenet, E.-M. Shih, J. Hone and T. F. Heinz, *Phys. Rev. B: Condens. Matter Mater. Phys.*, 2014, **90**, 205422.
13 N. Cavassilas, D. Logoteta, Y. Lee, F. Michelini, M. Lannoo, M. Bescond and M. Luisier, *J. Phys. Chem. C*, 2018, **122**, 28545–28549.
14 T. Roy, M. Tosun, X. Cao, H. Fang, D.-H. Lien, P. Zhao, Y.-Z. Chen, Y.-L. Chueh, J. Guo and A. Javey, *ACS Nano*, 2015, **9**, 2071–2079.
15 N. Oliva, J. Backman, L. Capua, M. Cavalieri, M. Luisier and A. M. Ionescu, *npj 2D Mater. Appl.*, 2020, **4**, 1–8.
16 Z. Zhou, X. Niu, Y. Zhang and J. Wang, *J. Mater. Chem. A*, 2019, **7**, 21835–21842.
17 K. Si, J. Ma, C. Lu, Y. Zhou, C. He, D. Yang, X. Wang and X. Xu, *Appl. Surf. Sci.*, 2020, **507**, 145082.
18 J. Wu, M. Liu, K. Chatterjee, K. P. Hackenberg, J. Shen, X. Zou, Y. Yan, J. Gu, Y. Yang, J. Lou and P. M. Ajayan, *Adv. Mater. Interfaces*, 2016, **3**, 1500669.
19 X. Yin, C. S. Tang, Y. Zheng, J. Gao, J. Wu, H. Zhang, M. Chhowalla, W. Chen and A. T. S. Wee, *Chem. Soc. Rev.*, 2021, **50**, 10087–10115.
20 Y. Fan, J. Wang and M. Zhao, *Nanoscale*, 2019, **11**, 14836–14843.
21 J. Shen, Y. He, J. Wu, C. Gao, K. Keyshar, X. Zhang, Y. Yang, M. Ye, R. Vajtai, J. Lou and P. M. Ajayan, *Nano Lett.*, 2015, **15**, 5449–5454.
22 M. M. Bernal, L. Álvarez, E. Giovanelli, A. Arnáiz, L. Ruiz-González, S. Casado, D. Granados, A. M. Pizarro, A. Castellanos-Gomez and E. M. Pérez, *2D Mater.*, 2016, **3**, 035014.
23 M. Cao, L. Ni, Z. Wang, J. Liu, Y. Tian, Y. Zhang, X. Wei, T. Guo, J. Fan and L. Duan, *Appl. Surf. Sci.*, 2021, **551**, 149364.
24 D. Wickramaratne, L. Weston and C. G. Van de Walle, *J. Phys. Chem. C*, 2018, **122**, 25524–25529.
25 A. Rousseau, L. Ren, A. Durand, P. Valvin, B. Gil, K. Watanabe, T. Taniguchi, B. Urbaszek, X. Marie, C. Robert and G. Cassabois, *Nano Lett.*, 2021, **21**, 10133–10138.
26 S. Latini, K. T. Winther, T. Olsen and K. S. Thygesen, *Nano Lett.*, 2017, **17**, 938–945.
27 O. Karni, E. Barré, S. C. Lau, R. Gillen, E. Y. Ma, B. Kim, K. Watanabe, T. Taniguchi, J. Maultzsch, K. Barmak, R. H. Page and T. F. Heinz, *Phys. Rev. Lett.*, 2019, **123**, 247402.
28 N. Sharma, H. Ma, T. Bottein, M. Bugnet, F. Vocanson, D. Grosso, T. E. Itina, Y. Ouerdane and N. Destouches, *J. Phys. Chem. C*, 2019, **123**, 6070–6079.
29 Q. Li, J. Lu, P. Gupta and M. Qiu, *Adv. Opt. Mater.*, 2019, **7**, 1900595.
30 K. T. Fountaine, H. J. Lewerenz and H. A. Atwater, *Nat. Commun.*, 2016, **7**, 13706.
31 M. A. Green, *Prog. Photovoltaics*, 2012, **20**, 472–476.
32 K. T. Fountaine, H. J. Lewerenz and H. A. Atwater, *Appl. Phys. Lett.*, 2014, **105**, 173901.
33 H. J. Conley, B. Wang, J. I. Ziegler, R. F. Haglund, S. T. Pantelides and K. I. Bolotin, *Nano Lett.*, 2013, **13**, 3626–3630.
34 M. Bernardi, M. Palummo and J. C. Grossman, *Nano Lett.*, 2013, **13**, 3664–3670.
35 B. A. Pinaud, J. D. Benck, L. C. Seitz, A. J. Forman, Z. Chen, T. G. Deutsch, B. D. James, K. N. Baum, G. N. Baum, S. Ardo, H. Wang, E. Miller and T. F. Jaramillo, *Energy Environ. Sci.*, 2013, **6**, 1983.
36 M. Grüning, A. Marini and A. Rubio, *J. Chem. Phys.*, 2006, **124**, 154108.